ISRN LUTMDN/TMHP—09/5199—SE
ISSN 0282-1990

Characterization of gas transport inside a package

Madeleine Jonsson

Thesis for the Degree of Master of Science

Division of Fluid Mechanics
Department of Energy Sciences
Faculty of Engineering, LTH
Lund University
P.O. Box 118
SE-221 00 Lund
Sweden

Characterization of gas transport inside a package

Abstract

A study of a sterilizing flow in a package is done. The study is done with the commercial code Fluent using Large Eddy Simulation and validated with both Laser Induced Fluorescence and Particle Image Velociometry.

The velocity field is examined in several ways; with changes in grid size, inlet conditions and sub-grid scale models. The study showed that the most important parameter is the size and form of the control volumes. A comparison with the PIV data shows that the simulations have lower velocity in the lower part of the package and more turbulent fluctuations in the whole package.

The concentration study is done with two different geometries, a larger with a 7 percent larger volume than the smaller. The grids of the two geometries differs in the way that the small package has only hexahedral cell and the large package also has some tetrahedral cells in the bottom. A comparison to LIF data shows that the simulations of the small package match really well both in the top and in the bottom of the package. The simulations of the large package match well in the top but have a lower concentration level at the bottom. This could be explained by the tetrahedral cells which generate more numerical diffusion. A comparison between the large and the small package shows only a small difference of concentration over time.

Contents

Nomenclature

Latin characters

a_{ij}	Reynold-stress anisotropy
C	concentration of an additive
C_μ	k- ε-model konstant
C_s	Smagorinsky constant
$\mathcal{C}_{ij}^{\circ}$	cross stresses
d	diameter of the pipe
D	diffusivity
G	filter function
$\hat{G}$	transfer function
k	kinetic energy
k_r	residual kinetic energy
L_e	entrance length
l_0	characteristic length
l_s	Smagorinsky length scale
$\mathcal{L}_{ij}^{\circ}$	Leonard stresses
p	pressure
r	radius
R	radius of the pipe
$\mathcal{R}_{ij}^{\circ}$	SGS Reynolds stresses
S_{ij}	rate of strain tensor
$\bar{\mathcal{S}}$	characteristic filtered rate of strain
t	time
T_{ij}	residual stress
u	velocity along x-axis
u_0	characteristic velocity
u_c	velocity at centeraxis
u_m	mean velocity
u_η	Kolmogorov velocity scale
u'	r.m.s of turbulent fluctuation along x-axis
v	velocity along y-axis
v'	r.m.s of turbulent fluctuation along x-axis
V	volume
w	velocity along z-axis
w'	r.m.s of turbulent fluctuation along x-axis

Greek characters

δ_{ij}	Kronecher-delta

Δ	filter width
ε	dissipation rate
η	Kolmogorov length scale
κ	wavenumber
λ	Taylor micro scale
μ	dynamic viscosity
ν	kinematic viscosity
ν_T	turbulent kinematic viscosity
ν_r	eddy viscosity
ρ	density
τ_{ij}	residual stress tensor
ϕ	arbitrary scalar

Dimensionless numbers

Re	Reynolds number
Sc	Schmidt number

1 Introduction

1.1 Background

This thesis is a study of a sterilizing flow. The studied application is a part of the Ready-To-Fill chain, see Figure 1.1. A system in which the package goes from empty to filled and sealed.

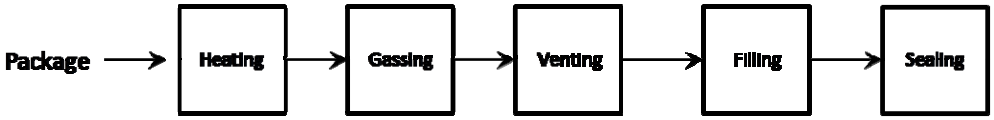

Figure 1.1: Ready-To-Fill chain

Before filling the package must be sterilized. The package is sterilized with hydrogen peroxide, H_2O_2, and is done in three steps:

- Heating
- Gassing
- Venting

The heating step is to avoid condensation of H_2O_2. In the gassing step, which is considered in this work, the package is filled with H_2O_2 and in the venting step the H_2O_2 is removed. In the gassing step the idea is to reach a desired concentration everywhere in the package in a short time and then let the H_2O_2 work until all the bacteria are gone. To optimize the gassing time Computational Fluid Dynamics, CFD, can be used to get the needed information; placement of the nozzle, velocity of the gas etc.[1]

In the historical point of view CFD is very young; the first "real" CFD calculation was done in the 1930s, and was a numerical solution of flow past a cylinder. The big breakthrough of CFD came in the 1960s and 1970s when several of the methods used today were developed. Since the 1980s when the first commercial CFD codes came out on the market the use of CFD has grown rapidly and are now used in all industries, from food packaging to designing airplanes.[2]

1.2 Objectives

The objective of the thesis is to do a numerical examination of a sterilization flow in a package using Large Eddy Simulation, LES, in Fluent. The aim is to gain more understanding of the sensitivity in the simulations of a confined turbulent jet to parameters such as inflow boundary conditions, subgrid-scale

model and grid size. Furthermore to understand how these parameters affect the concentration build-up.

The results are to be verified with Particle Image Velociometry, PIV, and Laser Induced Fluorescence, LIF.

1.3 Focus

The focus of this thesis is the numerical simulation. The simulations are done with the software Fluent, and the model used is LES. A small part of the work has been to participate in the experiments and learn a bit about LIF. The experiments are done at Tetra Pak, in a water rig.

1.4 Disposition

The theory of turbulence is written in chapter 2, the turbulence model used is also described here. The two techniques used in the experimental part, and the water rig are described in chapter 3. The different case setups are described in chapter 4, with some theory of the discretization schemes. The results are shown in chapter 5 and some conclusions are stated in chapter 6.

2 Theory

In this chapter the most important theory behind this thesis are described.

2.1 Governing equations

The behavior of an incompressible viscous flow is described by the continuity equation (2.1) and the momentum equation (2.2).

$$\frac{\partial u_i}{\partial x_i} = 0 \tag{2.1}$$

$$\frac{\partial u_i}{\partial t} + u_j \frac{\partial u_i}{\partial x_j} = -\frac{1}{\rho}\frac{\partial p}{\partial x_i} + \nu \frac{\partial^2 u_i}{\partial x_j \partial x_j} \tag{2.2}$$

In the equations above p is the pressure, ρ the density and ν is the kinematic viscosity. [3]

The mass transport of an additive is described by

$$\frac{\partial C}{\partial t} + u_j \frac{\partial C}{\partial x_j} = D \frac{\partial^2 C}{\partial x_j \partial x_j}, \tag{2.3}$$

where C is the concentration of the additive and D the molecular diffusivity.[4]

2.2 Pipe flow

The inlet conditions in a turbulent jet are determined by several parameters. One important parameter is the velocity profile in the nozzle, which is determined by the geometry upstream. The development of the profile is described here.

Flows in circular pipes behave different depending on the Reynolds number. The velocity profile is different for laminar and turbulent flows. The profile for a turbulent flow could empirically be described by

$$\frac{u_m}{u_c} = \left(1 - \frac{r}{R}\right)^{1/n} \tag{2.4}$$

The coefficient n varies with the Reynolds number. For fully turbulent flows the coefficient is between n=6 and n=10.

The velocity profile is depending on the geometry upstream. If there is a bend or a sudden reduction of width, the flow needs time to get a fully developed velocity profile. For turbulent profiles the following expression gives an approximate entrance length.

$$\frac{L_e}{d} \approx 4.4 Re_d^{1/6} \tag{2.5}$$

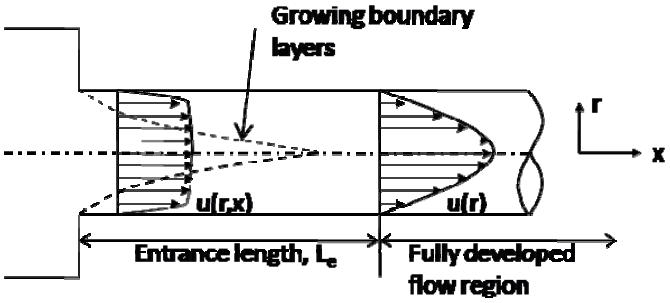

Figure 2.1: Entrance length in a pipe [3]

Figure 2.1 shows the development of the velocity profile after a sudden reduction of diameter. As the boundary layers grow due to friction at the walls the velocity profile gets a rounder and more laminar form. [3]

2.3 Turbulence

Turbulence is not a fluid property; it describes the flow of the fluid. Turbulence is characterized by the following properties. [5], [6]

- **High Reynolds number** – At the critical Reynolds number, Re_c, the flow turns from laminar to turbulent, transitional flow. At higher Reynolds number the flow is strictly turbulent.

- **Irregular** – Turbulent flow is irregular and can therefore not be fully determined; instead the flow is described statistically.

- **Diffusive** – A highly diffusive flow is spreading rapidly, which is an important feature when mixing fluids.

- **Dissipative** – Turbulent flow has large losses, without constant energy supply the turbulence will die out.

- **Rotational** – The flow must have a non-zero vorticity to be turbulent, it must also be 3-D.

- **Continuum phenomena –** The length scales of turbulence is always much bigger than the molecular length scale.

- **Property of the flow –** Turbulence is a property of the flow, not the fluid.

2.3.1 Statistical description

Turbulence is random, this means that an event can occur but it does not need to occur. The randomness of turbulence can cause major changes in the solution when making small changes in the outline.[7]

The velocity in a turbulent flow is time-dependent, and very fluctuating [7]. At a constant supply of energy the flow will later on become *statistically stationary*; this means that under a shift of time the statistics are invariant. Turbulence can also be *statistically isotropic*; then the flow is *statistically homogenous*, all fluctuations are invariant under a shift in space, and also invariant under rotation and reflection of the coordinate system.[8]

2.3.2 Transition

When a high speed flow enters into a stationary fluid, shear stresses arise along the interface between them. The shearing causes the stationary fluid to start moving and forces vortexes to roll up, as seen in Figure 2.2. The vortices start pairing up and bigger and stronger vortices forms. Then the big vortices breaks down into eddies of different size, and the flow is fully turbulent.[9]

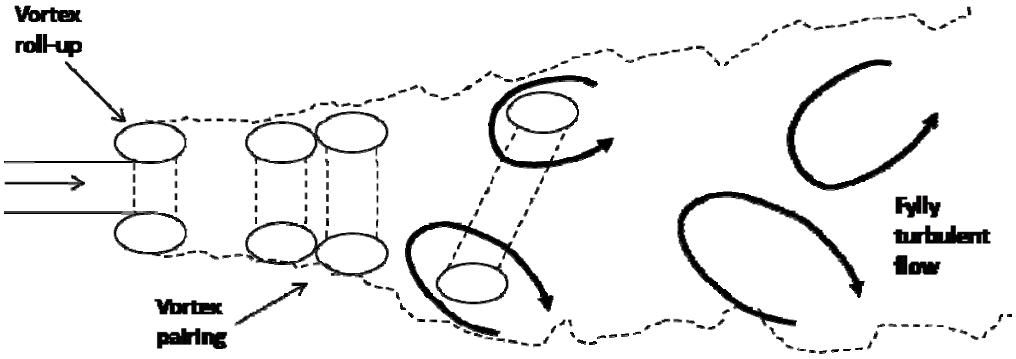

Figure 2.2: Transition in a round jet [9]

2.3.3 Scales of turbulent flows

Turbulence is composed of eddies, turbulent motions, of different sizes, from big energy containing eddies to small dissipative eddies. Figure 2.3 shows a schematic diagram of the energy cascade. Energy is transferred from the large scales to the smaller ones and then dissipated at the smallest scales.

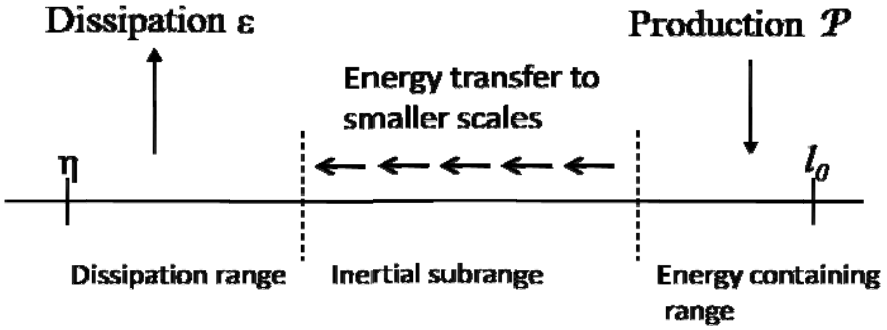

Figure 2.3: Energy cascade [7]

The length scale of the largest eddies, l_0, is determined by the local domain size. The magnitude of the velocity scale of the largest scales, $u_0=u(l_0)$, can be estimated by the velocity fluctuations, $u' \sim \sqrt{(2/3)k}$. In these eddies the turbulent Reynolds number, Re_0, is very high and therefore not directly affected by viscosity.[7]

$$Re_0 = \frac{u_0 l_0}{\nu} \sim Re \tag{2.6}$$

The smallest scale of turbulence, the Kolmogorov scale, can be described by Kolmogorovs 0th and 1th hypotheses. These two hypotheses state that small scale turbulence is locally isotropic and that it is determined only by viscosity, ν, and dissipation rate, ε. With these statements the smallest length scale is defined as $\eta = (\nu^3/\varepsilon)^{1/4}$ and the velocity is defined as $u_\eta = (\varepsilon\nu)^{1/4}$. Reynolds number for the Kolmogorov scales is equal to one.

$$Re_\eta = \frac{\eta u_\eta}{\nu} = 1 \tag{2.7}$$

Between the *energy containing range* and the *dissipating range* one can find the *inertial subrange*. This is just an energy transporting zone in which the large eddies are broken down into smaller ones. In the middle of the inertial subrange the Taylor microscale, λ, is found. In LES, since turbulence of

smaller scale can be seen as isotropic, the grid size can be chosen to be close to the Taylor microscale.

Energy transfer from small scales to larger scales can occur, that is a phenomenon called backscatter. [7], [8]

2.4 Turbulence modeling

There are several ways to solve the turbulent flow. It can be done by a Direct Numerical Simulation which takes lot of computational effort and time, but resolves all the length scales, see Figure 2.4.

With the wavenumber along the x-axis and the energy along the y-axis the different scales can be found in the energy spectrum. The slope in the inertial subrange is given by Kolmogorovs hypotheses, the assumption that all scales in the inertial subrange are uniquely determined by ε. The energy-spectrum function is

$$E(\mathrm{K}) = C\varepsilon^{2/3}\kappa^{-5/3}, \tag{2.8}$$

where C is a constant.

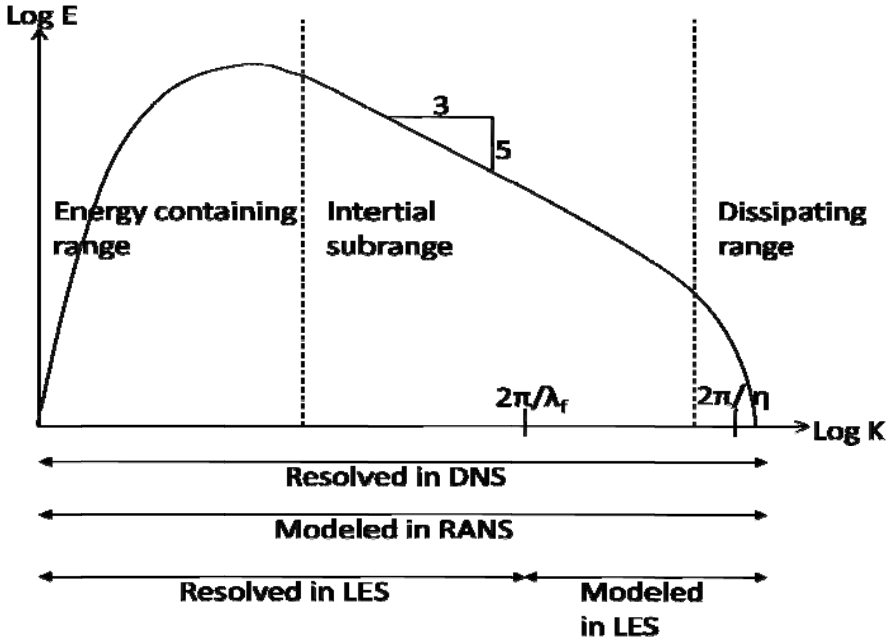

Figure 2.4: Energy spectrum [8]

Reynolds Averaged Navier-Stokes models solves the decomposed and time-averaged governing equations, this is the easiest and most common way to

solve the turbulent flow. A combination of modeling and resolving is Large Eddy Simulation. LES resolves the large scales and models the small scales. [7], [8]

2.4.1 Reynolds Average Navier-Stokes models

RANS models are based on modeling of the Reynolds stress tensor. The Reynolds stress tensor, eq. (2.9) is generated by decomposing and time-averaging the governing equations.

$$\overline{u'_\iota u'_\jmath} = \begin{bmatrix} \overline{u'^2} & \overline{u'v'} & \overline{u'w'} \\ \overline{v'u'} & \overline{v'^2} & \overline{v'w'} \\ \overline{w'u'} & \overline{w'v'} & \overline{w'^2} \end{bmatrix} \tag{2.9}$$

Velocity and pressure are decomposed in the same way. Figure 2.5 shows how velocity is decomposed into one steady mean part, $\bar{u}$, and one fluctuating part, u'. [7], [5]

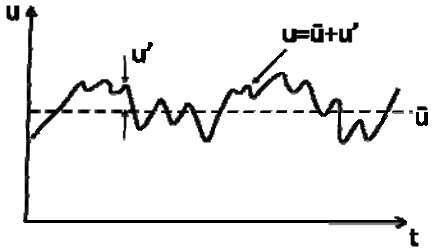

Figure 2.5: Definition of the decomposed velocity [6]

The appearance of the Reynolds stress tensor in the averaged momentum equations causes an unclosed system of governing equations that can not be solved numerically unless the Reynolds stress tensor is modelled This can be achieved by using a turbulent viscosity model based on Boussinesq's hypotheses. Modeling Boussinesq's hypotheses is based on the assumption that there is a linear relation between the Reynolds stress anisotropy,

$$a_{ij} \equiv \overline{u'_\iota u'_\jmath} - \frac{2}{3} k \delta_{ij} \tag{2.10}$$

and the mean velocity gradients, $\partial \overline{u_\iota} / \partial x_j$.

$$\overline{u'_\iota u'_\jmath} - \frac{2}{3} k \delta_{ij} = -\nu_T \left(\frac{\partial \overline{u_\iota}}{\partial x_j} + \frac{\partial \overline{u_\jmath}}{\partial x_i} \right) \tag{2.11}$$

Boussinesq's hypotheses can be used in many different cases, but there are several cases where the hypotheses fail, for example in flows with strong rotation, curved streamlines or secondary flow.

One common RANS models is the k-ε-model. The k-ε-model is a two equation model where the turbulent viscosity is:

$$\nu_T = C_\mu \frac{k^2}{\varepsilon} \tag{2.12}$$

To close the system, the modeled equations for kinetic energy and dissipation is needed. The k-ε-model is widely used and incorporated in most commercial software.[7], [8]

2.4.2 Large Eddy Simulation

LES is based on spatial filtering thereby large scales are resolved and small scales needs to be modeled. A common way to do this is to use an eddy-viscosity model.

The general filtering operation of velocity is defined by

$$\overline{\boldsymbol{u}}(\boldsymbol{x}, t) = \int G(\boldsymbol{r}, \boldsymbol{x}) \boldsymbol{u}(\boldsymbol{x} - \boldsymbol{r}) d\boldsymbol{r}, \tag{2.13}$$

where $G(\boldsymbol{r}, \boldsymbol{x})$ is the filter function, which should satisfy the normalization condition.

$$\int G(\boldsymbol{r}, \boldsymbol{x}) = 1 \tag{2.14}$$

The decomposed velocity is then given by

$$\boldsymbol{u}(\boldsymbol{x}, t) = \overline{\boldsymbol{u}}(\boldsymbol{x}, t) + \boldsymbol{u}'(\boldsymbol{x}, t) \tag{2.15}$$

In comparison with the Reynolds decomposition the filtered residual is not zero:

$$\overline{\boldsymbol{u}'}(\boldsymbol{x}, t) \neq 0 \tag{2.16}$$

The filtering can be done with different filtering operations. The three most common filters are the box filter, the Gaussian filter and the sharp spectral filter. In Table 2.1: Some common filter functions the filtering functions for

those three are given in one dimension form and they are depicted in Figure 2.6.[7]

Table 2.1: Some common filter functions[1]

Name	Filter function
Box	$\frac{1}{\Delta} H\left(\frac{1}{2}\Delta - \lvert r\rvert\right)$
Gaussian	$\left(\frac{6}{\pi\Delta^2}\right)^{1/2} exp\left(-\frac{6r^2}{\Delta^2}\right)$
Sharp spectral	$\frac{\sin(\pi r/\Delta)}{\pi r}$

The box filter and the Gaussian filter are positive filters and the sharp spectral is not, see Figure 2.6. In physical space the box filter is local and is non-local in wavenumber space, the sharp spectral filter is instead non-local in physical space and local in wavenumber space. As seen in Figure 2.6 the Gaussian filter is non-local in both spaces.[7],[10]

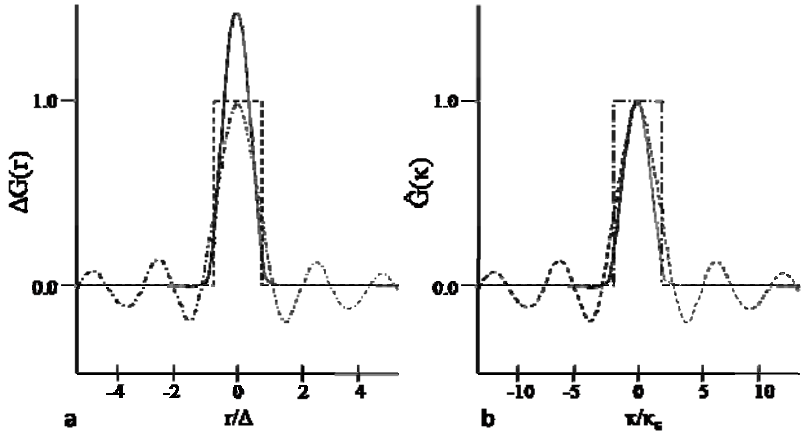

Figure 2.6: a) Filters G(r); box filter - dashed line, Gaussian filter - solid line and sharp spectral filter - dot-dashed line, b) Filter transfer functions $\hat{G}(\kappa)$; box filter - dashed line, Gaussian filter - solid line and sharp spectral filter - dot-dashed line [7]

In Fluent the filtering operation is implicitly provided by the finite-volume discretisation.

$$G(\boldsymbol{x},\boldsymbol{r}) = \begin{cases} 1/V, & \boldsymbol{r} \in \boldsymbol{\mathcal{V}} \\ 0, & \text{otherwise} \end{cases}, \tag{2.17}$$

where V is the volume of the computational cell.[11]

Filtering of the governing equations, (2.1) and (2.2), will result in

$$\frac{\partial \bar{u}_i}{\partial x_i} = 0 \tag{2.18}$$

$$\frac{\partial \bar{u}_i}{\partial t} + \frac{\partial \bar{u}_j \bar{u}_\iota}{\partial x_j} = -\frac{1}{\rho}\frac{\partial \bar{p}}{\partial x_i} + \nu \frac{\partial^2 \bar{u}_i}{\partial x_j \partial x_j} - \frac{\partial \tau_{ij}^r}{\partial x_j} \tag{2.19}$$

where the anisotropic residual stress tensor, τ_{ij}^r, is defined by

$$\tau_{ij}^r = \tau_{ij}^R - \frac{2}{3} k_r \delta_{ij} \tag{2.20}$$

$$\tau_{ij}^R = \overline{u_\iota u_j} - \bar{u}_j \bar{u}_\iota \tag{2.21}$$

τ_{ij}^R, the residual stress tensor can be composed into three parts according to Germano:

$$\tau_{ij}^R = \mathcal{L}_{ij}^{\mathrm{o}} + \mathcal{C}_{ij}^{\mathrm{o}} + \mathcal{R}_{ij}^{\mathrm{o}} \tag{2.22}$$

The three parts are the *Leonard stresses,* $\mathcal{L}_{ij}^{\mathrm{o}}$, the *cross term stresses,* $\mathcal{C}_{ij}^{\mathrm{o}}$, and the *SGS Reynolds stresses,* $\mathcal{R}_{ij}^{\mathrm{o}}$. In Figure 2.7 the different regions for the decomposed stresses in the energy spectrum are seen.

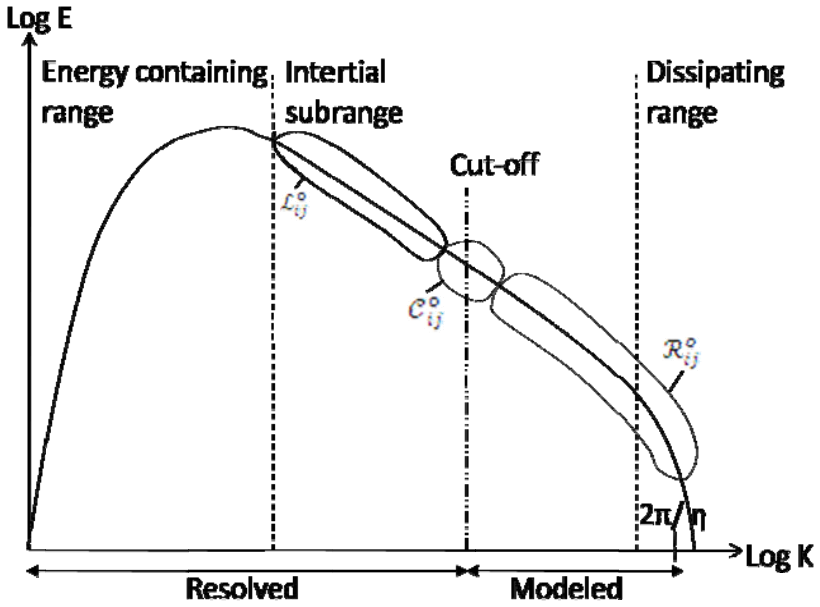

Figure 2.7: Energy spectrum with the decomposed stresses [7]

The Leonard stresses represent the interactions between the large resolved scales and they are

$$\mathcal{L}_{ij}^{o} = \overline{\overline{u}_\iota \overline{u}_\jmath} - \overline{\overline{u}}_\iota \overline{\overline{u}}_\jmath \,, \tag{2.23}$$

,the cross term stresses represent the interactions between scales around the cut-off and are

$$\mathcal{C}_{ij}^{o} = \overline{\overline{u}_\iota u'_\jmath} + \overline{u'_\iota \overline{u}_\jmath} + \overline{\overline{u}}_\iota \overline{u'}_\jmath + \overline{u'}_\iota \overline{\overline{u}}_\jmath \,, \tag{2.24}$$

and the SGS Reynolds stresses represent the interactions between the small resolved scales and are

$$\mathcal{R}_{ij}^{o} = \overline{u'_\iota u'_\jmath} + \overline{u'}_i \overline{u'}_\jmath \tag{2.25}$$

To model the small scales a subgrid-scale model is used. The models used in this thesis are the *Smagorinsky-Lilly model* and the *dynamic Smagorinsky-Lilly model.*

The Smagorinsky-Lilly model is an eddy-viscosity model where the residual stresses relates to the filtered rate of strain, $\overline{S_{\iota\jmath}}$, as

$$\tau_{ij}^{r} = -2\nu_r \overline{S_{ij}} \,. \tag{2.26}$$

The eddy viscosity, ν_r, is modeled as

$$\nu_r = l_S^2 \bar{\mathcal{S}} = (C_S \Delta)^2 \bar{\mathcal{S}} \,, \tag{2.27}$$

$$\bar{\mathcal{S}} = (2\overline{S_{ij}}\,\overline{S_{ij}})^{1/2}. \tag{2.28}$$

$\bar{\mathcal{S}}$ is the absolute value of rate of strain and l_S is the Smagorinsky length scale which is proportional to the filter width, Δ. The constant C_S is the Smagorinsky coefficient. The coefficient C_S is derived by Lilly and usually around 0.1. The Smagorinsky-Lilly model does not account for backscatter.

The dynamic Smagorinsky-Lilly model is basically the same as the above. But the coefficient C_S is not specified; instead it is calculated locally by the information given by the resolved scales. Two filtering operations with different filter widths are done instead of one. The first is the *grid filter,* with the filter width $\bar{\Delta}$ and the second is the *test filter* with the filter width $\tilde{\Delta}$.This results in two new filtering operations,

$$\bar{\boldsymbol{u}}(\boldsymbol{x}, t) = \int G(|\boldsymbol{r}|; \bar{\Delta}) \boldsymbol{u}(\boldsymbol{x} - \boldsymbol{r}, t) d\boldsymbol{r} \tag{2.29}$$

for the grid filter and

$$\tilde{\bar{\boldsymbol{u}}}(\boldsymbol{x}, t) = \int G\big(|\boldsymbol{r}|; \tilde{\Delta}\big) \boldsymbol{u}(\boldsymbol{x} - \boldsymbol{r}, t) d\boldsymbol{r} \tag{2.30}$$

for the test filter. The residual stresses for the double filtered equations are defined by

$$T_{ij} = \widetilde{\overline{u_i}\,\overline{u_j}} - \tilde{\bar{u}}_i \tilde{\bar{u}}_j. \tag{2.31}$$

In the dynamic Smagorinsky-Lilly model the residual stresses, τ_{ij}^{r}, are written

$$\tau_{ij}^{r} = -2c_s \bar{\Delta}^2 \bar{\mathcal{S}} \bar{S}_{ij}. \tag{2.32}$$

The constant ${C_S}^2$ is here changed to c_s, and can therefore be negative and take in to account for backscatter. The residual stresses for the double filtered grid is written

$$T_{ij} = -2c_s\tilde{\bar{\Delta}}^2\tilde{\bar{S}}\tilde{\bar{S}}_{ij}\,. \tag{2.33}$$

The dynamic model is very accurate for high-Reynolds-number turbulence and provided that the filter widths are well within the inertial subrange, where the assumption that the Smagorinsky length scale is proportional to the filter width.[7]

3 Experimental setup

To verify the simulations done in Fluent, laser-based experiments were conducted in a water rig. Two techniques were employed, Laser Induced Fluorescence, LIF, was used to verify the spreading of species and hence the mixing process and Particle Image Velocimetry, PIV, for visualization of the velocity field. A schematic picture of the experimental setup is seen in Figure 3.1, the same rig being used in both experiments.

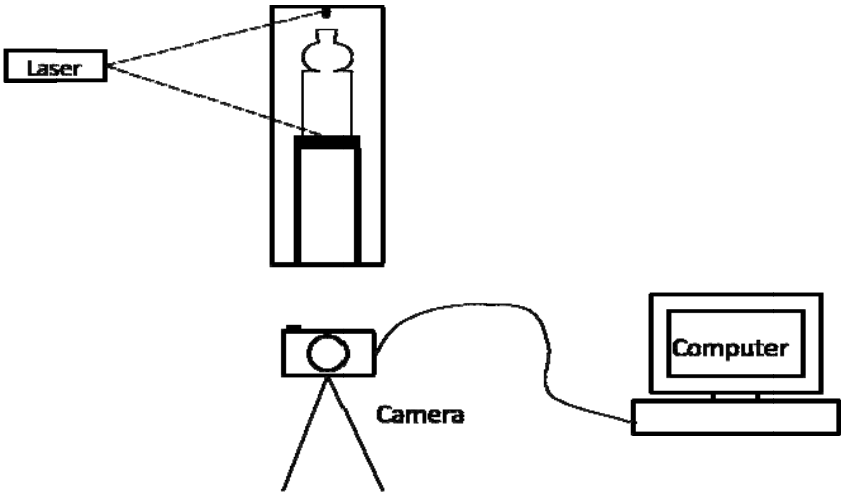

Figure 3.1: Schematic picture of the water rig

The chamber with the bottle is connected to a closed water loop. The water loop contains a water tank, a pump and a flow-meter. When a measurement starts a valve above the chamber opens and let the water into the chamber through the nozzle. For the LIF experiments the injected water was seeded with a fluorescent species (Rhodamine) which is fully resolved in the water. In the PIV experiments small seeding particles were added to the flow.

3.1 Laser Induced Fluorescence

Laser Induced Fluorescence is used to map concentration or temperature. When mapping concentration a fluorescent substance, Rhodamin 6G, is added to the water.

When a laser pulse hits a molecule of Rhodamin, the molecule absorbs the energy from the laser radiation and is excited to a higher energy level, see Figure 3.2. The higher level of excitement is unstable and the molecule will return to the ground level. When returning to the ground level of excitement the electron emits light radiation, i.e. flourescence, only from the first level of excitement, therefore with a longer wavelength. The intensity of the emitted

light is proportional to the concentration of the fluorescence and is then measured.

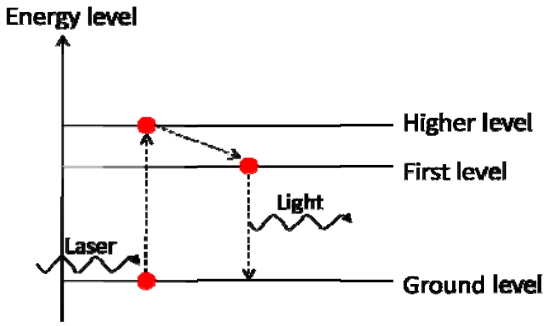

Figure 3.2: Energy jump [13]

The emitted light is captured by a high speed camera, which is equipped with a filter that keeps out wavelengths shorter than the emitted ones. The images from the camera are then post-processed to get the desired information.[12], [13]

3.2 PIV

Particle Image Velociometry is used to map the velocity field of a flow. The velocity is found by tracing the displacement of particles at a given time interval, $dt = t_2 - t_1$. The tracer particles added to the flow should follow the motions of the flow.

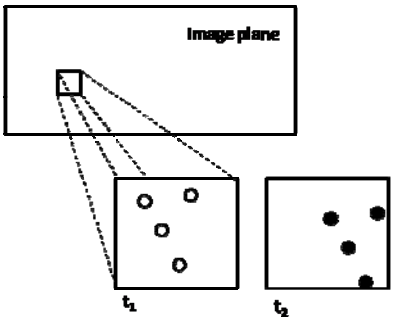

Figure 3.3: Displacement of particles [13]

To trace the small particles a double pulsed laser is used. The laser pulses illuminates the particles with the given time interval and the reflected light is captured with a camera. The image plane given by the camera, Figure 3.3, is divided into small domains for which the velocity is calculated. The displacement vector for each domain between t_1 and t_2 is obtained by

calculating the cross-correlation. With a displacement vector $\boldsymbol{dx}$ the velocity is given by:[12], [14]

$$u = \frac{d\boldsymbol{x}}{dt} \tag{3.1}$$

4 Numerical setup

4.1 Grid

The grid used in this thesis is generated with the commercial software Gambit. A model, made in ProEngineer, of the package was used to build up the computational domain. To get an indication of the size of the cells some simulations with the k-ε-model was done. For these simulations an unstructured tetrahedral mesh was used.

The grid size can, as said in 2.3.3, be set as the Taylor microscale. With k and ε from the k-ε-simulation, the Taylor microscale can be approximated as [5]

$$\lambda \approx \left(10\frac{\mu}{\rho}\frac{k}{\varepsilon}\right)^{1/2}. \tag{4.1}$$

The computational domain is built up with structured hexahedral volumes. Due to the geometry of the package some parts of the domain is done with unstructured tetrahedral volumes. For better resolution some parts has been adapted. The adaptation makes one element into eight. In Figure 4.1 three different grids used are specified. The first configuration, Standard, has one volume adaptation, from the nozzle down to the waist. The second, Standard +, is adapted the same way as the Standard but all the way down to the tetrahedral cells. The third configuration has a second adaptation in the middle of the bottle.

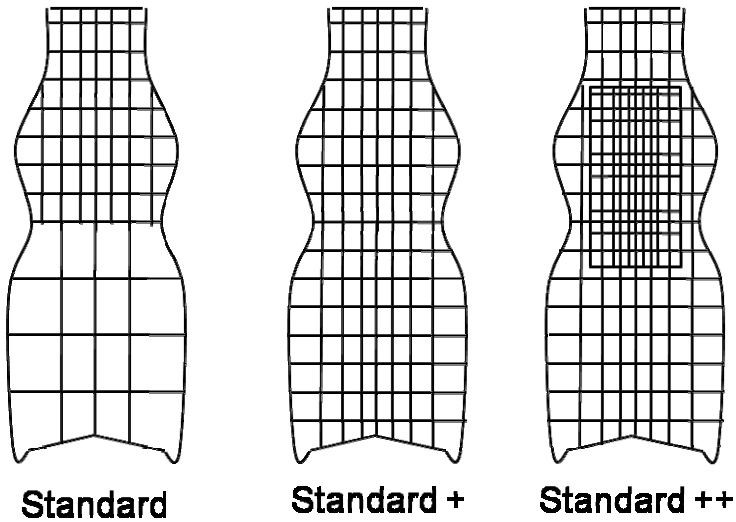

Figure 4.1: The three grid configurations; Standard, Standard+ and Standard++

The mesh is done in two parts, one with the nozzle and one with the bottle. In an optimization study one will save time if only a small part of the whole domain needs to be remeshed. The two meshes are made separately in Gambit and then connected in Fluent. The cells of the two interfaces do not have an exact match, so the information that crosses the interface will be interpolated where needed.

4.2 Discretisation schemes

Solving the transport problem in Fluent the finite volume method (FVM) is used. When using this method the Navier-Stokes equations are rewritten to get algebraic expressions that can be solved numerically.

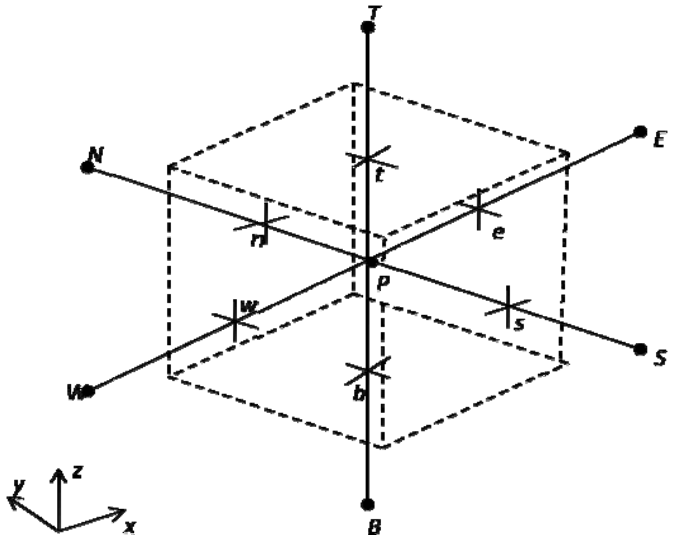

Figure 4.2: Three dimensional control volume [9]

The discretisation schemes used in these simulations are combinations of three more common ones which will be described here for the one dimensional case. Same procedure is done for the other two dimensions. In Figure 4.2 the faces and nodes of a three dimensional control volume is visualized. The cell with the central point *P* has the six neighboring points east, west, north, south, top and bottom. The nodes and faces in the descriptions below are those along the x-axis, east and west. [9]

First-order upwind

In the first-order upwind scheme the values of face *e* and *w* is sets equal to the values at the upstream nodes *W* and *P*. This scheme is stable in highly convective flows but also very diffusive due to numerical diffusion.[9]

$$\phi_w = \phi_W$$
$$\phi_e = \phi_P \tag{4.2}$$

Second-order upwind
The second-order upwind scheme is based on the same idea as the first-order scheme, but to get higher accuracy a second-order Taylor expansion is made. This gives the following expression for the face value:[9]

$$\phi_{e,SOU} = \phi_P + \frac{\partial \phi_P}{\partial x} \cdot dx_{Pe}\,, \tag{4.3}$$

The second-order upwind scheme generates a less diffusive result than the first-order upwind.

Central differencing
In Fluent the central differencing scheme is of second-order accuracy. Central differencing scheme is a linear approximation that with the second-order accuracy takes into calculation the gradients at node *E* and *P*. [9]

$$\phi_{e,CD} = \frac{1}{2}(\phi_E + \phi_P) + \frac{1}{2}(\frac{\partial \phi_E}{\partial x} \cdot dx_{eE} + \frac{\partial \phi_P}{\partial x} \cdot dx_{Pe}) \tag{4.4}$$

4.2.1 Discretization of momentum

The momentum equations are solved with the bounded central differencing scheme. This scheme chooses from central differencing scheme, a combination scheme of central differencing and second-order upwind and also the first-order upwind scheme. The choice is based on two conditions; the convective boundness criterion (CBC) and normalized variable diagram (NVD). [11]

4.2.2 Discretization of mass transport

Solving the equations of mass transport the third-order MUSCL scheme is used. This is a combination of the central differencing scheme and second-order upwind scheme. The two schemes are weighted as follows [11]

$$\phi_e = \theta \cdot \phi_{e,CD} + (1 - \theta) \cdot \phi_{e,SOU}. \tag{4.5}$$

4.2.3 Discretization of pressure

The pressure is solved with the standard scheme; an interpolation of the pressure at the cell nodes is done to get the value of the cell face. The standard scheme is accurate for flows with small gradients in momentum. If the standard scheme is used in flows with a high gradient in momentum the result will be over- or undershoots in the cell velocity. [11]

4.2.4 Temporal discretisation

In transient simulations, the equations also need to be disctretizised in time. This is done with second order accuracy, for a variable ϕ the change in time is given by:

$$\frac{\partial \phi}{\partial t} = \frac{3\phi^{n+1} - 4\phi^{n} + \phi^{n-1}}{2\Delta t} \tag{4.6}$$

It is important that the time-step is small enough in transient simulations, if it is too big the solution will be incorrect. A criterion to get the time-step small enough is that the Courant–Friedrichs–Lewy number is less than one. [11]

$$CFL = \frac{u \cdot \Delta t}{\Delta x} \tag{4.7}$$

4.3 Solver

The solving algorithm used is Non-Iterative Time Advancement (NITA) with the velocity coupling scheme Fractional Step (FSM).

The NITA algorithm is used for transient simulations to speed up the simulation time. In a time advancing scheme all the equations are solved iteratively until the convergence criteria are met. The NITA scheme performs only a single outer iteration per time step. The equations are instead solved with smaller inner loops, one loop for each set of equations. To preserve the overall time accuracy the splitting error should be in the same order as the truncation error. A schematic picture of the NITA method is shown in Figure 4.3.

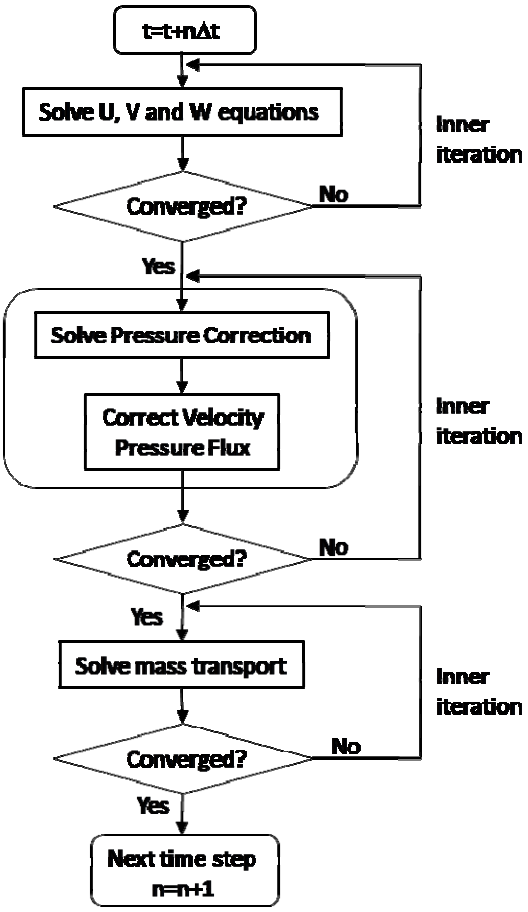

Figure 4.3: NITA Solution method [11]

The FSM scheme is a method to decouple the momentum equations from the continuity equation. This is done with a mathematical technique called operator-splitting. [11]

5 Case settings

There are nine different simulations done, all with different settings.

The Schmidt number for hydrogen peroxide is 1. To get better resemblance with the experiments the Schmidt number is set to 1250, the Schmidt number of Rodamine, and is same for all cases.

$$Sc = \frac{\nu}{D} \tag{4.8}$$

At the inlet the fluctuating velocity is modeled with the Vortex Method. This method adds a perturbation to the mean velocity profile in form of a fluctuating vorticity field [10].

The solution controls for the NITA scheme has four parameters that controls the inner iteration loops; maximal number of corrections, correction tolerance, residual tolerance and relaxation factor. The settings for the cases are seen in Table 5.1.

Table 5.1: NITA Solution Controls

	Max. corrections	Correction tolerance	Residual tolerance	Relaxation factor
Pressure	10	0.25	0.0001	1
Momentum	5	0.25	0.0001	1
Rhodamin	5	0.25	0.0001	1

Two different profiles are used in the simulations, one is a plug profile and one is a turbulent profile based on the entrance length, see 2.2. The plug profile is a mean velocity profile. The two profiles are illustrated in Figure 5.1.

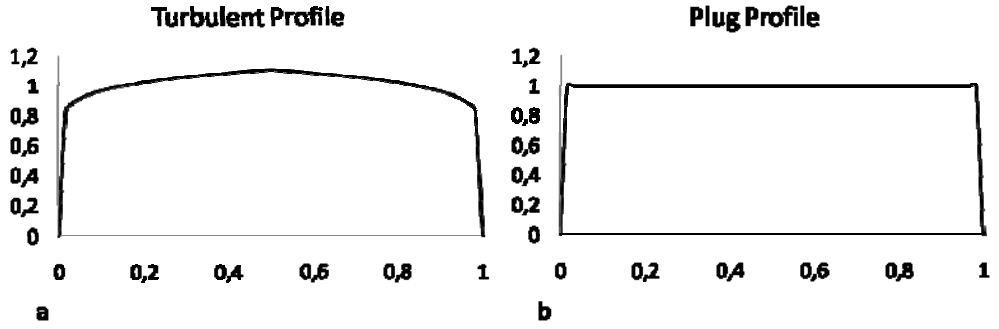

Figure 5.1: The a) turbulent velocity profile and b) plug velocity profile as function of nozzle diameter

The settings for the inlet for the nine different cases are summarized in the three tables below, one table for each grid configuration; Table 5.2 for Standard, Table 5.3 for Standard+ and Table 5.5 for Standard++. The chosen subgrid-scale model, SGS model, for each case can also be seen.

Table 5.2 Settings for the three Standard cases

	Vel 110%	**Turb Int 1**	**Turb Int 5**
SGS	Dyn Smag	Dyn Smag	Dyn Smag
Turbulent Intensity [%]	5	1	5
Velocity [-]	1.1	1	1
Profile	Plug	Plug	Plug

For the Standard configuration the aim is to see how changes in turbulent intensity and in velocity profile at the affect the velocity field downstream.

Table 5.3: Settings for the four Standard + cases

	Smag	**Dyn Smag**	**Profil**	**Dyn Smag +**
SGS	Smag	Dyn Smag	Dyn Smag	Dyn Smag
Turbulent Intensity [%]	5	5	5	5
Velocity [-]	1	1	1	1
Profile	Plug	Plug	Turb Profile	Plug

The study of the Standard+ configuration is focused on how the velocity field is affected by the sub-grid scale model, by the inlet boundary condition (plug profile or turbulent profile) and by data-sampling-time and changes in the NITA solver controls affects the mean values. The changes in the NITA solver control are for the maximum corrections and the residual tolerance, see Table 5.4.

Table 5.4: : NITA Solution Controls for Dyn Smag +

	Max. corrections	Correction tolerance	Residual tolerance	Relaxation factor
Pressure	15	0.25	0.00001	1
Momentum	10	0.25	0.00001	1
Rhodamin	5	0.25	0.00001	1

The last configuration, Standard++, has two setups; the Dyn Smag, with the plug profile, and Profil+, with a turbulent profile and an extra refinement of the tetrahedral cells in the bottom of the bottle.

Table 5.5: Settings for the two Standard++ cases

	Dyn Smag	**Profil+**
SGS	Dyn Smag	Dyn Smag
Turbulent Intensity [%]	5	5
Velocity [-]	1	1
Profile	Plug	Turb Profile

The concentration study is done for two different geometries, one larger and one smaller. The large package has a 7 percent larger volume than the small package. The concentration build up is examined at four points in the package; in the upper part and in the lower part, see Figure 5.2.

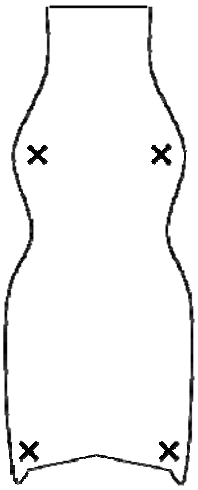

Figure 5.2: The examined points in the simulations

6 Results

In this chapter all results are presented. The first part is an examination of the grid sensitivity, the second part discusses the velocity field and how changes of different parameters affect the field, and the third part is a study of the concentration field, how it is affected by the geometry of the package.

6.1 Grid

6.1.1 Interface

The interface between the two parts is set at y/d=0.6. As can be seen in Figure 6.1 vortices are only generated on the left side of the jet. At the interpolation over the interface information from three cells is put into one cell. Important information is lost here and the jet behaves unphysically.

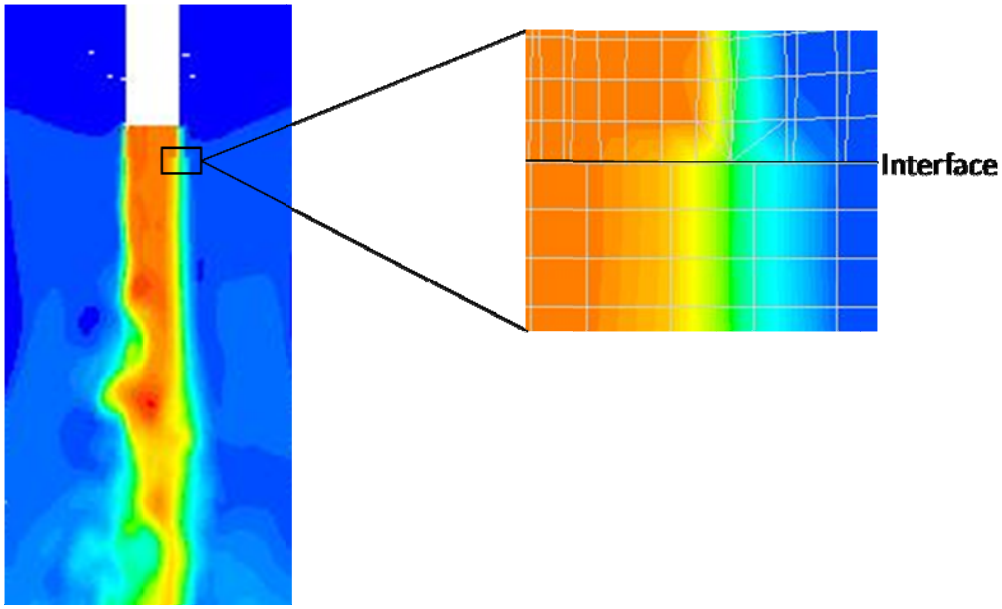

Figure 6.1: Interpolation problem

To get a more physical jet the mesh had to be remade. The interface was moved down to y=5d, into the package, so that the core of the jet would not be affected by the interpolation.

6.1.2 Cell size

Figure 6.2 shows the energy spectrum at four different points in the computational domain and are based on the velocity in the direction normal to the inlet. The spectrums are taken from “Profil” which has the “Standard+”

configuration. The dashed lines in the plots are equal to the -5/3 slope that states the inertial subrange. The four points are shown in Figure 6.3.

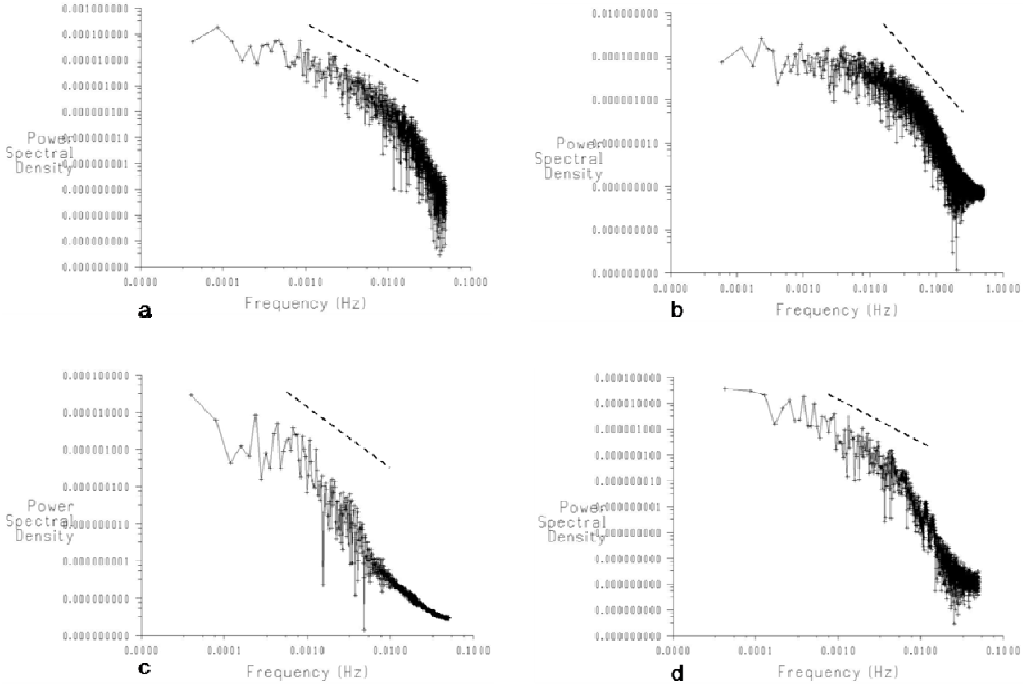

Figure 6.2: Energy spectrum based on the velocity in the direction normal to the inlet at a) p2, b) p1, c) p4 and d) p3.

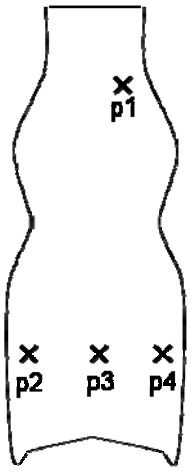

Figure 6.3: Positions of the points p1, p2, p3 and p4

A comparison of the spectrums and the dashed lines in each plot shows that at all points the grid size is well within the inertial subrange and therefore small enough for the simulations.

6.2 Velocity

The velocity field for all cases is examined along three lines; the centerline, from the nozzle to the bottom and across the package at y/d=12.56 and y/d=19.64 from the nozzle.

6.2.1 Standard

In the "Standard" case a change of inlet velocity and a change of turbulent intensity were made. The results from these simulations are seen in Figure 6.4-Figure 6.6.

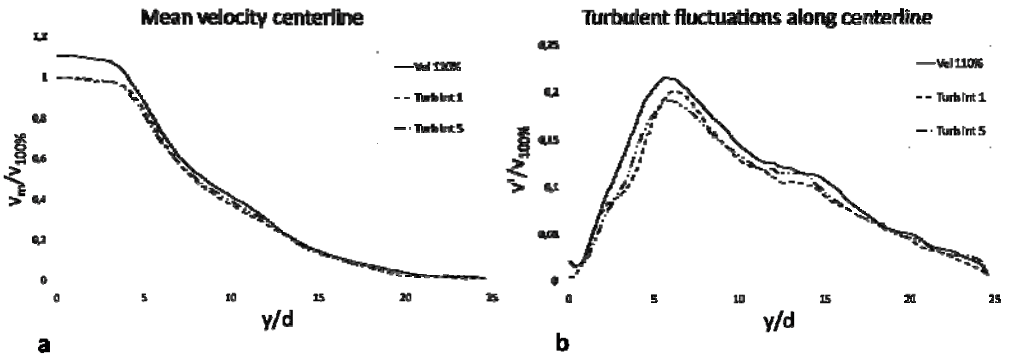

Figure 6.4: a) Mean velocity and b) turbulent fluctuations along centerline

As seen in Figure 6.4 a change of turbulent intensity from 1% to 5% neither affects the mean velocity nor the turbulent fluctuations along the centerline. The increase of velocity at the inlet affect the mean velocity field somewhat, the mean velocity is slightly higher in the upper part of the package for the case "Vel 110%". With the higher velocity the turbulent fluctuations also gets higher.

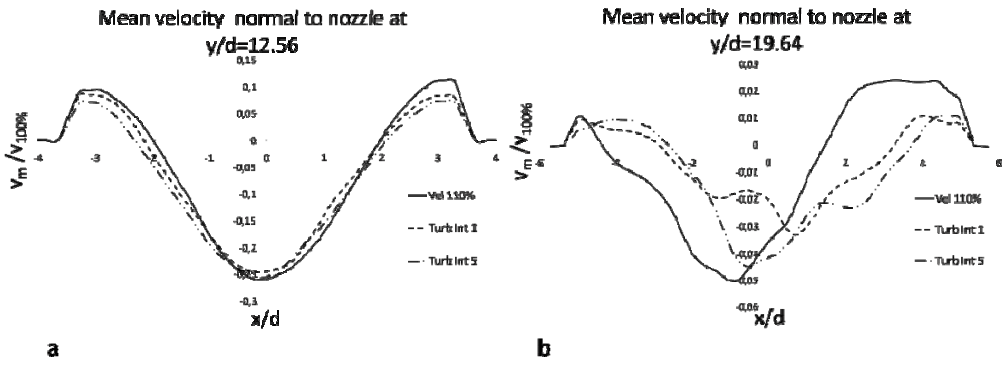

Figure 6.5: Mean velocity along x-axis at a) y/d=12.56 and b) y/d=19.64

In Figure 6.5a the velocity profile has almost the same appearance for all three cases in compare with Figure 6.5b where the velocity profiles differs quite a bit from case to case, a small difference of top velocity can be seen between "Turb Int 1" and "Turb Int 5". The irregularity of the plots at y/d=19.64 depends on a too short mean value sampling interval.

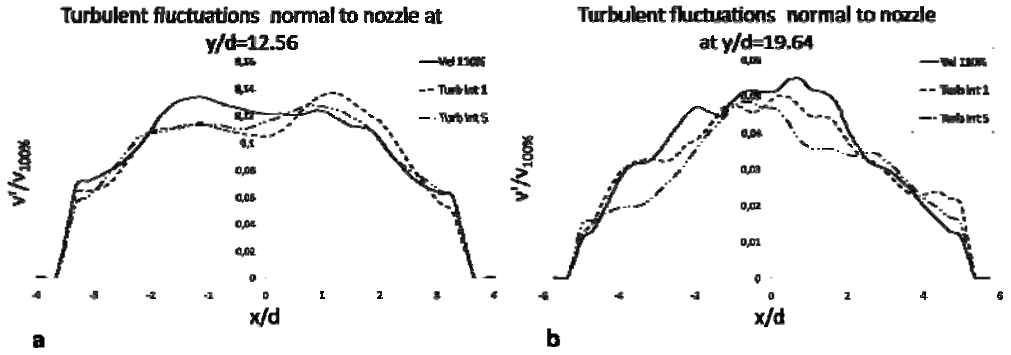

Figure 6.6: Turbulent fluctuations along x-axis at a) y/d=12.56 and b) y/d=19.64

The plot in Figure 6.6a shows that the turbulent fluctuations for the three cases are of the same size and have the same profile at y/d=12.56. In the lower part of the package the "Vel 110%" case have somewhat higher fluctuations than the other two cases due to the higher inlet velocity.

The small difference of velocity in Figure 6.5b indicates that the turbulent intensity change at the inlet affects the velocity downstream, lower turbulent intensity at inlet cause lower velocity in the bottom of the package. Common for all the cases is the low velocity in the bottom of the package, although the case "Vel 110%" has the higher velocity at the inlet the velocity has dropped to the same level as the other cases at y/d=12.56.

6.2.2 Standard+

Four cases were studied with the "Standard+" configuration; the aim is to see how change of profile, change of subgrid-scale model and how a change of convergence criteria and longer mean value sampling time affects the velocity field. The results are seen in Figure 6.7-Figure 6.9.

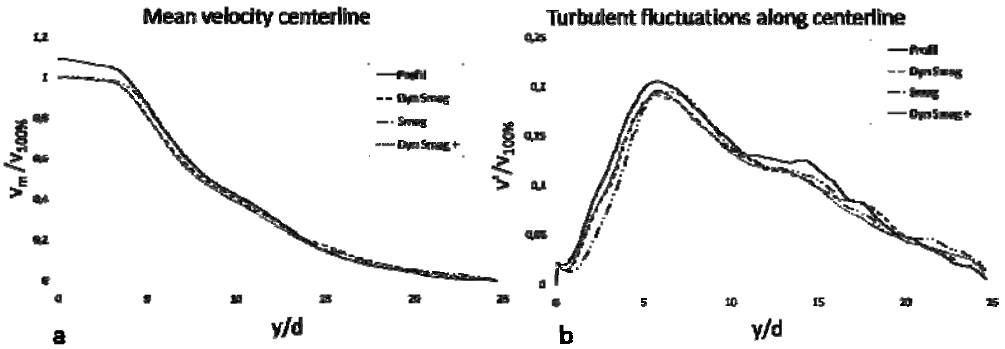

Figure 6.7: a) Mean velocity and b) turbulent fluctuations along centerline

The plots in Figure 6.7 show that the mean velocity along the centerline is not affected by the changes made; the change of profile is only seen in the first five diameters. The turbulent fluctuations on the other hand are a bit higher for the turbulent profile case than the others.

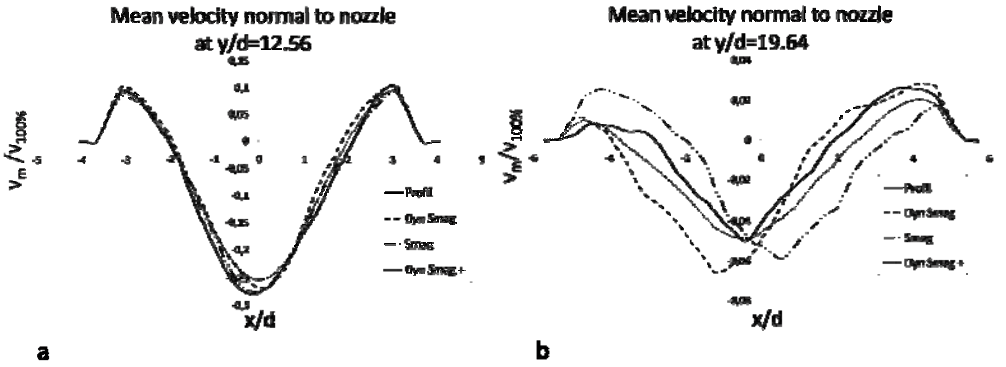

Figure 6.8: Mean velocity along x-axis at a) y/d=12.56 and b) y/d=19.64

At y/d=12.56 all the cases have the same velocity profile as seen in Figure 6.8a. In Figure 6.8b the difference in data-sampling time can be seen on the smoother velocity profile for the "Dyn Smag+" case, with lower velocities longer sampling time is needed to get converged results.

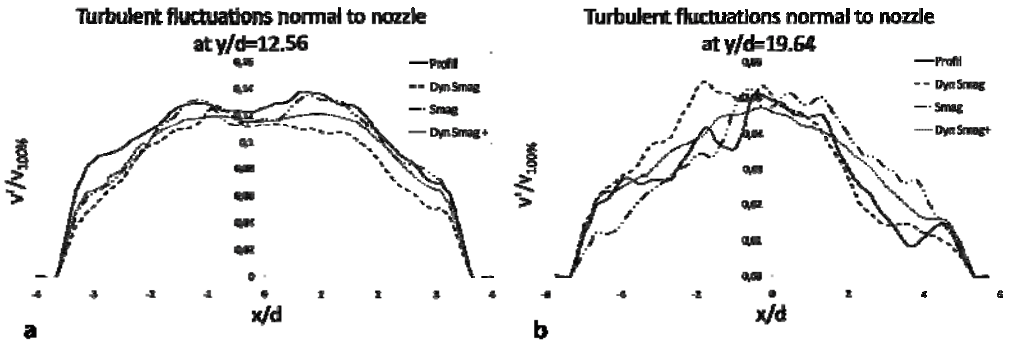

Figure 6.9: Turbulent fluctuations along x-axis at a) y/d=12.56 and b) y/d=19.64

The turbulent fluctuations in Figure 6.9a are all of the same size and have the same form. The irregular profiles for "Profil", "Dyn Smag" and "Smag" in Figure 6.9b are due to insufficient sampling time.

The change of subgrid-scale model from Dynamic Smagorinsky-Lilly to Smagorinsky-Lilly does neither affect the velocity field nor the turbulent fluctuations. The change to a turbulent profile results in the most distinct change of the velocity field. With a higher centerline velocity and more fluctuations in the upper part of the package it dissipates energy which results in a lower velocity and less fluctuations in the bottom of the package. A comparison between "Dyn Smag" and "Dyn Smag+" shows how much the mean velocity field depends on the data-sampling time, more time gives a more converged velocity field.

6.2.3 Standard++

The "Standard++" configuration is used for two cases; one with a standard plug profile and one with a turbulent profile and a refinement of the tetrahedral cells in the bottom of the package. The results from these two simulations are represented by Figure 6.10 and Figure 6.11.

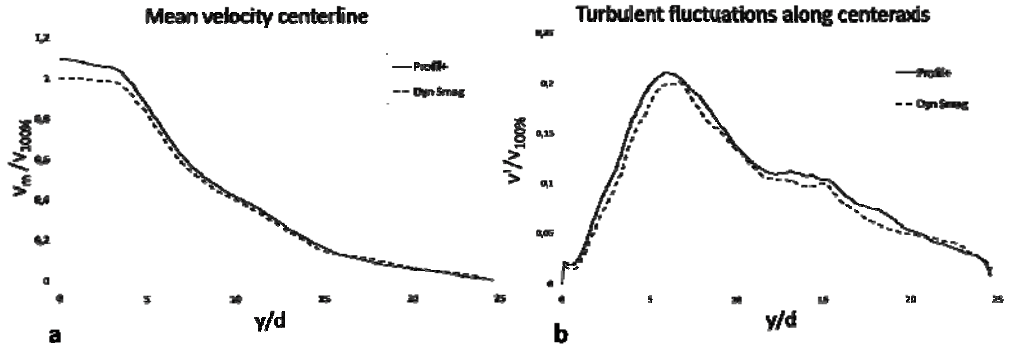

Figure 6.10: a) Mean velocity and b) turbulent fluctuations along centerline

Figure 6.10a shows that a change of profile will give a slightly higher centerline mean velocity, this can be explained by the higher center velocity of the turbulent profile; 1.1 compared to 1. In Figure 6.10b the RMS velocity for the case with the turbulent profile is a bit higher than for the plug profile case, due to the higher center velocity.

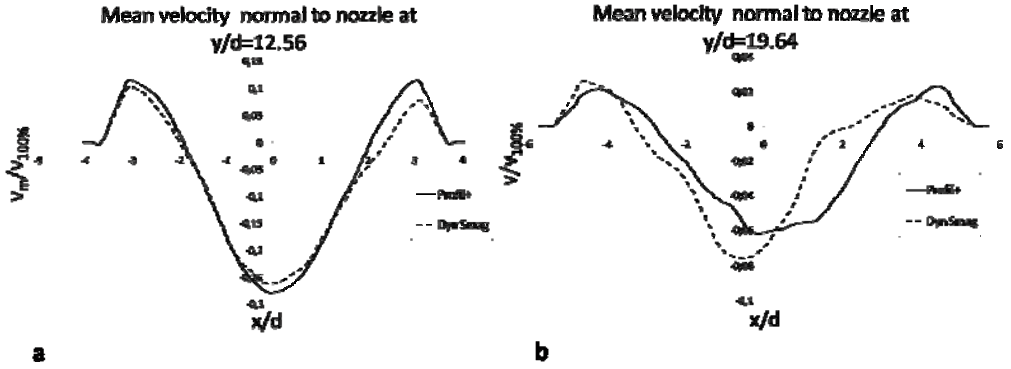

Figure 6.11: Mean velocity along x-axis at a) y/d=12.56 and b) y/d=19.64

The velocity profiles at y/d=12.56 are similar, both in shape and magnitude, as is seen in the Figure 6.11a. Further downstream at y/d=19 the "Dyn Smag" velocity profile has a bit higher center velocity than the "Profil+" (Figure 6.11b).

The change to the turbulent profile results in a higher centerline velocity and more turbulent fluctuations the first 15 diameters, but in the lower part of the package they both drop. The drop in velocity can depend on more dissipation in the upper part of the package where the fluctuations in the "Profil+"-case are larger.

6.2.4 Comparison

A comparison of all the nine cases shows only small differences in the velocity profile at y/d=12.56, the span of the center velocity is from 0.23 to 0.27, with the highest velocities for the "Standard++"-cases. At y/d=19.64 the same observation can be done. With velocities from 0.035 to 0.08 the difference between the cases is much larger. Same trend is observed when looking at the mean velocities along the centerline. The most important change done here is the refinement of the mesh; it shows clearly that small changes do not affect the velocity field as much as the change of grid size.

6.2.5 Validation

One of the methods examined is also compared to experimental data, to see how well it matches. The method chosen is the "DynSmag" and it is applied to a fine mesh with cells in the size of the "Standard++"-configuration cell size. The velocities and the turbulent fluctuations is examined along the same lines; centerline, y/d=12.56 and y/d=19.64. A major difference between the simulation and the experiment are the boundary conditions at the inlet. The only thing known about the inlet in the experiment is the velocity profile and the mean velocity.

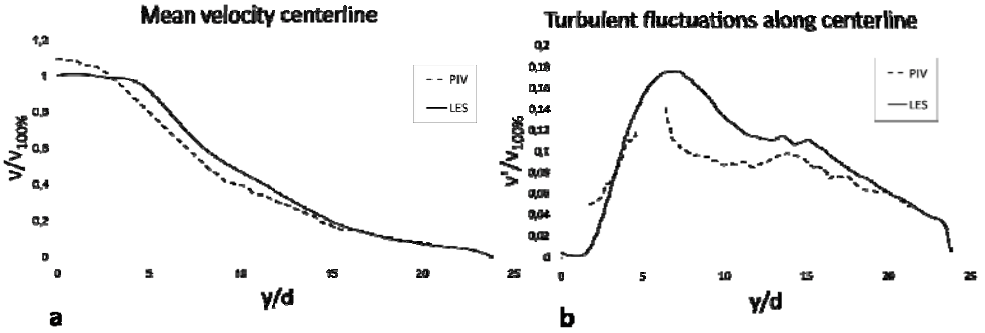

Figure 6.12: a) Mean velocity and b) turbulent fluctuations along centerline

In Figure 6.12a there is a small velocity difference at the inlet, which is due to the plug profile set at the inlet in the simulations. Also, the jet breaks up earlier in the experiments than in the simulations. The centerline velocity is a bit higher for the simulation from 5d to 15d into the package. The turbulent fluctuations along the centerline, Figure 6.12b, differ a lot between the simulations and the experiment.

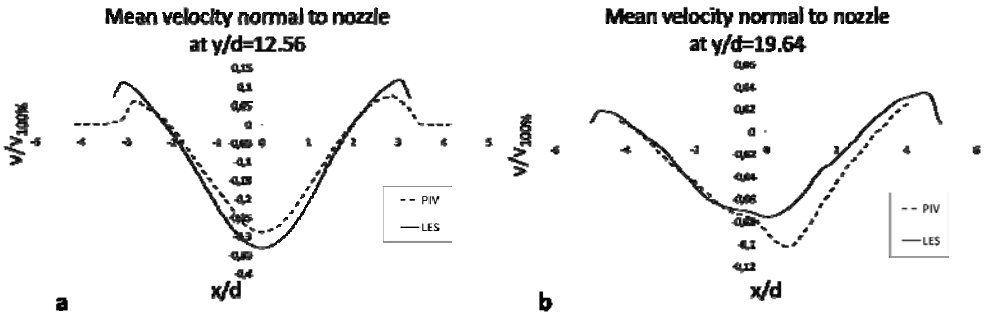

Figure 6.13: Mean velocity along x-axis at a) y/d=12.56 and b) y/d=19.64

The velocity profiles in Figure 6.13 shows that the velocity of the simulation and the velocity of the experiment have almost the same profile and velocity through the whole package. The higher velocity of the experiment in Figure 6.13b can depend on an oblique velocity structure in the bottom of the package.

Since the velocities are taken in just one plane the velocity profile from another plane could have a different shape.

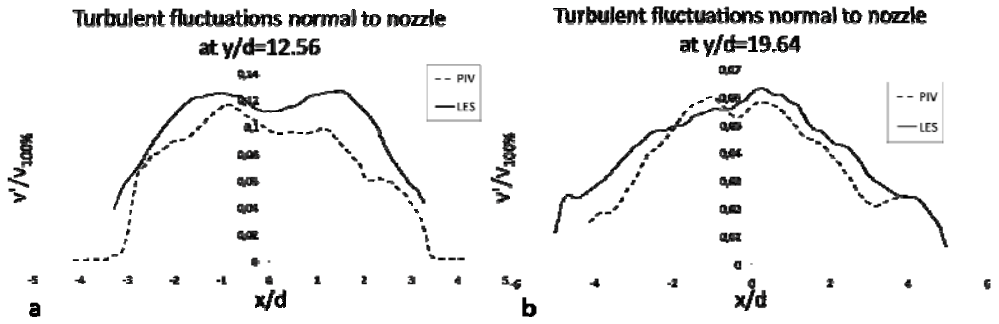

Figure 6.14: Turbulent fluctuations along x-axis at a) y/d=12.56 and b) y/d=19.64

The turbulent fluctuation plots in Figure 6.14a shows larger values for the simulation than the experiment. Higher turbulent fluctuations lead to a better mixing. In the bottom of the package the turbulent fluctuations from both the experiment and the simulation have a maximum value of about 0.06. The turbulent fluctuations from the simulations have a bit wider profile than the experiment, i.e. more activity across the package.

An important source of error is the laser and the geometry of the package, with a complex geometry the laser spreads when it hits the glass and the signal from the particles gets poor which makes it difficult to evaluate the results. This is seen in Figure 6.12b where the PIV-plot is cut from 5 to 7 diameters. The simulation on the other hand is more diffusive than the real case and that can explain the lower velocity in the lower part of the package.

6.3 Concentration

The concentration results are divided into two parts, first a comparison between the simulations and the experiments, then a comparison between the large package and the smaller package.

6.3.1 LES vs. LIF

The concentration is examined at two different points in the package in the experiments; one in the upper part and one in the lower part of the package, and at four different points in the package in the simulations; two in the upper part of the package and two in the lower part of the package. Two points are taken in the simulations to see if there is a change from side to side over the package.

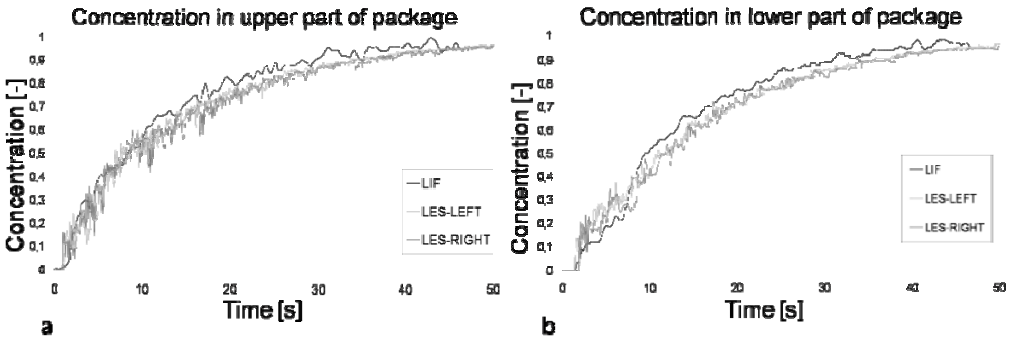

Figure 6.15: Concentration over time in the small package; a) upper part and b) lower part

In the small package the concentration build up from the simulation and the experiment match very well. In Figure 6.15a the concentration build up in the upper part of the package is shown, in the beginning of the process the concentration in the simulation match the results from the experiment very well. After about 10 seconds the concentration in the experiment increase faster than in the simulation, this can depend on more diffusion in the simulations. After 50 seconds the concentration level of both the simulation and experiment is converged at 0.98. In the lower part of the package, Figure 6.15b, same trend is seen, except a small difference in the beginning where the concentration level of the simulation increase a bit faster than in the simulation.

Seen in the velocity comparison between the experiment and the simulation, the profile for the turbulent fluctuations in the lower part of the package is much wider for the simulation. A wider profile leads to more diffusion.

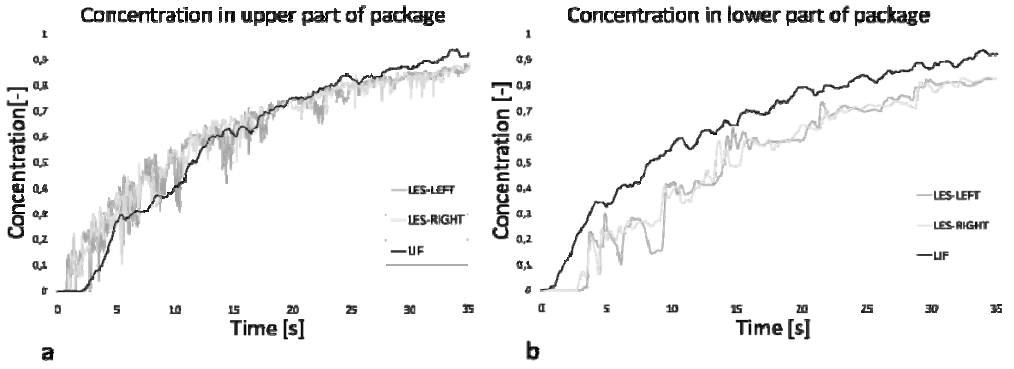

Figure 6.16: Concentration over time in the large package; a) upper part and b) lower part

In the upper part of the large package, Figure 6.16a, the concentration build up in the simulation increase faster in the beginning comparing to the experiment.

At about 20 seconds the concentration level of the experiment and the simulation are the same. No converging level of the concentration can be seen due to too small time span. In Figure 6.16b another trend is seen, the concentration level of the simulation starts building up much later than the simulation. However a comparison between the two shows that the slope of the curves is almost the same. The lower concentration in the bottom of the package in the simulations can in this case depend on the tetrahedral cells in the bottom of the package which give rise to more numerical diffusion.

6.3.2 Large vs. Small

The two geometries are here compared both in the upper part of the package and in the lower part of the package.

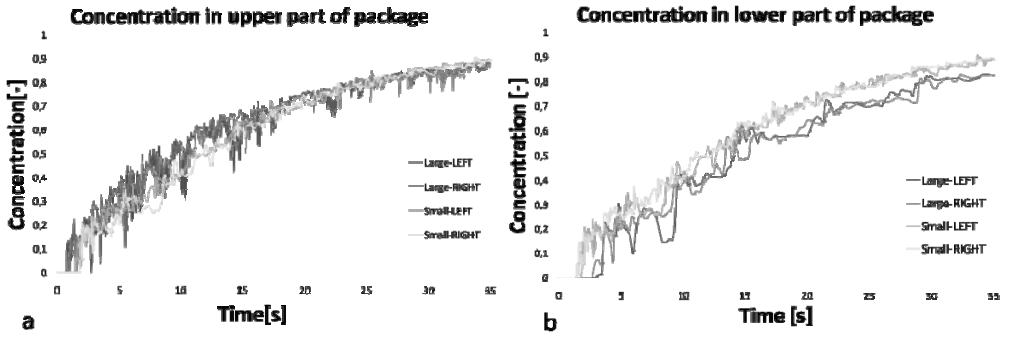

Figure 6.17: Concentration over time in package; a) upper part and b) lower part

Seen in Figure 6.17a is that the concentration level increase a bit faster in the large package in the beginning of the process until 20 seconds where the concentration level in the small package has caught up. After the compared 35 seconds both the simulations have a concentration level of 0.9. In the lower part of the package, Figure 6.17b, the concentration in the small package builds up much faster. With a difference of 0.08 after 35 seconds the concentration level in the lower part of the package still is higher in the small package.

Important in the comparison of the large and the small package is that the grid in the small package consists of hexahedral cells only whereas the grid of the large package has tetrahedral cells in the bottom of the package. The tetrahedral cells give rise to more numerical diffusion.

7 Conclusions

The study made in this thesis is an examination of a sterilizing flow in a package. Changes of parameters are done to see how they affect the velocity field and a geometry change is done to see how that affects the concentration field. The results from the simulations are compared to the results from the experiments which are to be seen as a reference case.

- The grid is of great importance, a finer grid with only cubic hexahedral cell gives a better result, since cells with less quality result in more diffusion.

- The mean velocity field is quite insensitive to small changes of the inlet conditions.

- A small change of geometry does not affect the concentration field.

8 Bibliography

[1] Michael Olsson, Tetra Pak, Private communication, January 2009

[2] www.fluent.com/about/cfdhistory.htm. "A Brief History of CFD". 2009-02-04

[3] White, Frank M. (1986) *"Fluid Mechanics"* McGraw-Hill, Second edition

[4] *"Compendia in Heat and Mass Transfer"* (2008) Division of Heat Transfer, Department of Energy Sciences, Lund Institute of Technology, Lund

[5] www.bakker.org/dartmouth06/engs150/. "CFD Class". 2009-02-04

[6] Norberg, Christoffer (2008) *"Turbulens- en introduktion"* Department of Energy Sciences, Lund Institute of Technology, Lund

[7] Pope, Steven B. (2000) *"Turbulent Flows"*, Cambridge University Press

[8] Johan Revstedt, Lund Institute of Technology, Turbulence: Theory and modeling, 2007

[9] Versteeg, H.K. & Malalasekera, W. (1995) *"An introduction to Computational Fluid Dynamics",* Prentice Hall

[10] Sagaut, Pierre (2006) *"Large Eddy Simulation for Incompressible Flows An Introduction"* Springer Verlag, Third Edition, Berlin Heidelberg

[11] *"Fluent 6.3 – User Guide"* (2006) Fluent Inc.

[12] Ding, Rong (2004) *"Experimental Studies of Turbulent Mixing in Impinging Jets"* Doctorial thesis, Division of Fluid Mechanics, Department of Heat and Power Engineering, Lund Institute of Technology, Lund

[13] Hans Seyfried, Tetra Pak, Private communication, Autumn 2008

[14] Raffel M., Willert C. & Kompenhans J. (1998) *"Particle Image Velocimetry"* Springer-Verlag, Third edition, Berlin Heidelberg